Biomedical Physics & Engineering Express

OPEN ACCESS

RECEIVED
2 September 2025

REVISED
22 January 2026

ACCEPTED FOR PUBLICATION
29 January 2026

PUBLISHED
14 April 2026

PAPER

Statistical modeling of blood and tissue signatures using ultrasonic color flow imaging

Atefeh Abdolmanafi[1,*], Jonathan M Rubin[1], Stephen Z Pinter[1], J Brian Fowlkes[1,2] and Oliver D Kripfgans[1,2]

[1] Department of Radiology, Michigan Medicine, University of Michigan, Ann Arbor, MI 48109-2026, United States of America
[2] Department of Biomedical Engineering, University of Michigan, Ann Arbor, MI 48109-2099, United States of America
[*] Author to whom any correspondence should be addressed.

E-mail: manafi@med.umich.edu

Keywords: color flow ultrasound, color flow power, statistical modeling, gamma distribution

Abstract

Conventional color flow processing is primarily optimized for qualitative visualization of flow dynamics, limiting its diagnostic use in regions where vascular structures are small relative to the ultrasound beamwidth. Leveraging the statistical properties of color flow data may provide a pathway toward quantitative discrimination between blood and tissue signals. This could enhance detection of vascular abnormalities, improve diagnostic accuracy, and support monitoring in diseases with small hemodynamic changes. Experimental data were obtained using a clinical GE LOGIQ 9 ultrasound system with a 10L linear array probe (3.75 MHz) positioned on an in-house made half-space flow phantom with the focus located at 3 cm depth. The simulation data obtained from Field II used a setup analogous to the experimental settings. Theoretical probability density function of ultrasound color flow power was derived using a gamma distribution. Shape parameters for blood and tissue were estimated using maximum likelihood estimation (MLE) in both simulation and experimental data. Color flow power was found to follow the gamma distribution in both simulation and experimental data. The estimated shape parameters aligned with theoretical predictions and distinguished between blood and tissue. Estimated shape parameters are less than or equal to 1 for tissue samples and greater than 1 for blood samples. This study presents a statistical modeling approach to enhance blood-tissue differentiation in color flow ultrasound, enabling blood characterization and perfusion quantification for improved detection and monitoring of vascular abnormalities.

1. Introduction

Undiagnosed changes in blood flow can have severe consequences, leading to disease or tissue death. Altered blood flow can cause organ damage, stroke, heart attack, and peripheral artery disease by depriving tissues of essential oxygen and nutrients [1]. Proper blood flow is essential for organ and tissue function, but it remains challenging to quantify it inexpensively and noninvasively.

Ultrasound has been widely employed for real-time visualization of blood flow using color flow imaging [2, 3]. While color flow imaging enables real-time flow visualization, quantification of blood flow requires additional insight into the underlying flow characteristics.

Using color flow power, established in [4], the integrated power spectrum of the received signal at each pixel can be measured, which is proportional to the moving red blood cells (RBC) in that area. This power measurement differs fundamentally from velocity, which is the mean radio frequency (RF)- or in-phase and quadrature (IQ)-signal phase shift produced by moving RBCs. The benefit of using power is its enhanced sensitivity to flow as well as its ability to suppress noise, which exhibits consistently low power. Additionally, color flow power is largely independent of angle [4].

Quantitative modeling of blood flow has been approached from both structural and statistical perspectives. Anatomical and computational blood flow modeling, such as multi-scale perfusion simulations and synthetic vascular networks [5, 6], provide insight into vascular health and tissue perfusion. Modeling the statistical behavior of color flow power offers a signal-based method for capturing flow heterogeneity and underlying physiological changes without the need for explicit anatomical mapping. A critical review on statistical modeling of ultrasound echo-envelope signals highlights the use of compound probability distributions such as Rice, Nakagami, K, and Homodyned-K to characterize signal amplitude, with particular emphasis on the gamma distribution for distinguishing speckle and coherent scattering components [7]. Shankar introduced a statistical model based on the Nakagami distribution to describe ultrasonic backscatter from tissues. This model offers a simpler and more versatile alternative to complex K-distributions, effectively capturing variations in scatterer density and structure. However, it is limited to static B-mode echo data [8]. In another study, Shankar introduced a generalized Nakagami distribution with three parameters to better model the statistics of ultrasonic backscatter echoes from tissue. This extension improves the fit over that of traditional two-parameter models like Rayleigh, K, and standard Nakagami distributions, especially in capturing the tail behavior [9]. In yet another study, Shankar proposed a compound probability density function for modeling the ultrasonic echo envelope, based on a gamma-gamma framework that accounts for both local and global variations in tissue scattering cross sections. This model unifies and generalizes the Rayleigh, K, and Nakagami distributions, offering greater flexibility in representing echo statistics under diverse scattering conditions [10]. Nillesen *et al* used speckle-based statistical modeling with Gamma and K distributions to detect the myocardium in echocardiographic B-mode images, aiming to improve segmentation. While scale and shape parameters enabled tissue separation, local estimation caused edge blurring, requiring adaptive filtering to preserve boundaries [11]. While these models have addressed tissue characterization, they have been applied to B-mode envelope data and lack direct validation in dynamic flow environments.

Another review study by Damerjian *et al* concentrated on various statistical and spatial methods for characterizing ultrasound speckle patterns. They outline several probabilistic models including Rayleigh, Rice, K, Homodyned-K, and generalized gamma distributions for modeling multiplicative speckle statistics. The authors highlight the effectiveness of generalized mixture models like the generalized gamma mixture. However, these methods effectively capture static tissue heterogeneity but are limited in investigating dynamic flow characteristics and differentiating between blood and tissue in motion-sensitive modes [12].

Al-Kadi *et al* introduced a multi-resolution Nakagami-based fractal descriptor to capture intra-tissue variations in 3D ultrasound data, improving tissue characterization beyond conventional single-scale models. While effective for B-mode texture analysis, it does not investigate the dynamic flow signal characteristics [13]. Oelze and Mamou reviewed quantitative ultrasound techniques, focusing on envelope statistics and backscatter coefficient imaging for tissue characterization. They highlight how statistical models (i.e., Nakagami, Homodyned-K) applied to echo-envelope data can quantify microstructural properties of tissue in a system-independent manner [14]. While powerful for B-mode imaging, these approaches were not used for blood flow characterization and flow-related signal variability. Teh and Cloutier modeled ultrasonic backscatter from RBC aggregates, including spherical clumps and rouleaux, showing that backscatter intensity varies with aggregate size, shape, and shear rate. Their work demonstrated that RBC aggregation enhances backscattered power, while shear dispersion reduces it, linking microstructural blood changes to signal behavior [15]. While their model is based on physical simulations of RBC morphology, it is not an anatomy-independent model and needs assumptions about the RBC aggregate structure and about flow geometry.

Müller *et al* compared color-flow imaging, power-based flow imaging, and peak systolic techniques for assessing carotid artery stenosis, demonstrating that both color flow and power modes provide reproducible measurements comparable to peak frequency shift, with accuracies exceeding 90%. This supports the clinical reliability of flow-derived power signals for vascular assessment [16]. However, the study focuses on large vessel diagnostics and stenosis quantification using anatomical thresholds. It does not address statistical characterization of signal heterogeneity or variations in flow behavior at finer spatial scales.

Statistical modeling of ultrasound RF or envelope signals has been widely investigated for tissue characterization, including generalized Gaussian and related models applied primarily to B-mode imaging under static scattering conditions [8, 12, 14, 17, 18]. In contrast, this study focuses on the statistical behavior of IQ-derived color flow power, which is formed by summing squared in-phase and quadrature components across the packet ensemble. As a result, color flow power is non-negative, more robust to noise, and largely angle-independent compared to velocity-based measures. Importantly, color flow power reflects dynamic scattering processes associated with blood motion and temporal decorrelation, rather than static tissue structure. These characteristics distinguish the proposed power-based statistical framework from prior RF-based speckle modeling

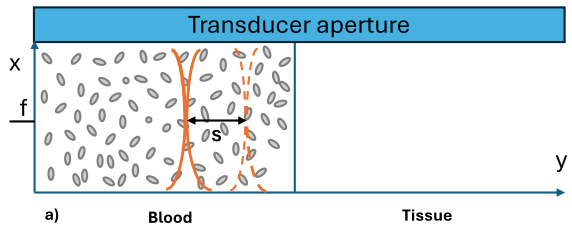

Figure 1. Illustration of the blood flow simulation setup. Axial-lateral side view of the soft-tissue / blood-lumen interface. Synthesized beams are focused to a depth f and spaced by s, based on their -6 dB (transmit / receive) beamwidths, with respect to their lateral FWHM at the focus (f).

approaches and highlight its relevance for flow imaging.

Color flow power statistics is integral to advancing the comprehensive analysis of hemodynamics and tissue morphology. Through the application of statistical techniques, diagnostically significant patterns within color flow power data can potentially be investigated. In this study, we investigate the following hypothesis using both simulation and experimental data: Color flow power derived from IQ data follows a gamma distribution, exhibiting distinct ranges of shape parameters for blood and tissue, as well as a continuous transition between blood and tissue.

2. Materials and methods

2.1. Simulation

Color flow analysis was performed on simulation data similar to previously generated RF data [19]. Field II simulation [20] was performed for a 128 element linear array probe at a 3.75 MHz center frequency and operating at an f-number of 3 (figure 1). Parameters were selected to match the clinical scanner setup. An f-number of 3 was chosen in the simulation to match the clinical color flow setting. The focal depth was set to 3 cm to match carotid and peripheral vascular applications. The color flow field was placed across the full aperture (3.9 cm laterally) and with a 1 cm axial range centered at the 3 cm focal position. While the L10 probe supports a higher color flow frequency of 5 MHz, we chose a color flow frequency of 3.75 MHz to operate the system at a lower spatial resolution but still within the settings of peripheral vascular use.

The middle of the aperture was placed at the interface from tissue to a blood vessel; the latter with a plug flow profile. Soft tissue and blood were simulated with 15 scatterers per resolution cell to achieve a Rician speckle distribution. Color flow data was obtained by sending and receiving an ensemble of acoustic tone bursts along a given scan line. The ensemble is often referred to as a packet. Sixteen firings were transmitted in each color flow packet at a pulse repetition rate of 0.8 kHz. Color velocity and power were computed according to the Kasai algorithm [21, 22]. Simulation was performed with blood signal levels set 40 dB below those of tissue to approximate signal levels seen *in vivo* and thus allowed us to isolate and analyze the statistical behavior of the signal under simulated clinical conditions. We simulated 50 scan volumes with 636 axial samples, and 104 lateral beams (first 52 beams in tissue, last 52 beams in blood). All beams were spaced by −6 dB (transmit/receive) with respect to their point spread function at the focus.

2.2. Experimental data

The experimental data was acquired using an in-house made half-space flow phantom that mirrors the simulation geometry. The tissue mimicking material formulation consisted of a mixture of gelatin (15%) and silicon dioxide (2%) inspired by [23]. A mass of 200 g of gelatin was dissolved in 1 L of distilled water to create an aqueous solution. Separately, 30 g of silicon dioxide were dissolved in 200 mL of distilled water in another container. Once both solutions were homogeneous and clear, they were combined and thoroughly mixed. The lumen was created by placing a 3D printed cuboid structure with lateral and elevational dimensions of 18 mm and 5 mm, respectively, which acts as a lumen stencil, and it was removed once the gelatin had set. This lack of a vessel wall also mirrored the simulation setup. Data collection was performed using the GE LOGIQ 9 ultrasound system with a linear array matching the simulation transducer (figure 2).

Blood-mimicking fluid (CIRS Doppler Fluid, model 769DF: Sound speed, 1570 ± 30 m s^{-1}; Attenuation, 0.1 ± 0.05 dB cm-MHz^{-1}; Density, 1.01–1.09 g mL^{-1}; Viscosity, 4.0 ± 0.5 mPa.s) was mixed for 3 hours before each use to ensure homogeneous particle distribution, prevent settling or clumping, and maintain consistent acoustic properties. Additionally, we allowed the fluid to circulate for one hour prior to imaging to eliminate air bubbles and ensure stable acoustic conditions. We recorded three IQ datasets, spaced 2 hours apart, each consisting of 50 cine loops with 44 frames each. The color flow box was centered on the focus with a height and width of 1 cm and 3.9 cm, respectively. This resulted in 66 and 262 axial and lateral voxels, and therefore a

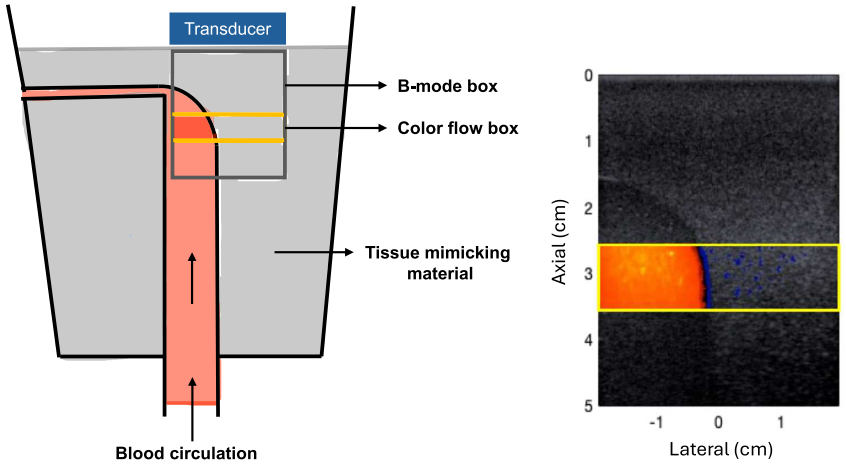

Figure 2. Left: Experimental setup using a custom-built half-space flow phantom designed to replicate the simulation geometry. The tissue-mimicking material was composed of 15% gelatin and 2% silicon dioxide. A 3D-printed cuboid stencil (18 mm × 5 mm) was used to form the lumen and removed after the gelatin solidified, resulting in a wall-less channel consistent with the simulation. Data were acquired using a GE LOGIQ 9 ultrasound system with a 10L linear array transducer matched to the simulation setup. Right: Color flow power superimposed on B-mode. The yellow box is indicating the color flow box position.

data set of 50 × 66 × 262 × 44 samples. Experimental data were acquired under conditions similar to the simulation setup, with tissue signals dominating over blood. No wall filter was applied to the simulation and experimental data. This choice was made to preserve the original statistical structure of the color flow power signal and to avoid introducing filter-dependent modifications to the power distribution. By analyzing unfiltered IQ-derived power, we aim to isolate the statistical differences between blood and tissue arising from their respective scattering dynamics. While wall filtering is commonly used in color flow, its effects on the statistical properties of power signals should be addressed in future studies. Note that here blood refers to blood-mimicking fluid and tissue refers to tissue mimicking material.

2.3. Statistical analysis

As introduced in [24], the derivative of the instantaneous phase, i.e., the phase difference between the two temporally adjacent samples divided by the time between them when averaged across the packet, produces, an estimate of the mean angular phase shift caused by blood motion. These phase shifts can be written as a complex sinusoid $e^{i\Delta\phi} = e^{i\omega_{CF}\Delta t}$. $\Delta\phi$ represents the phase difference between the two consecutive firings separated by time Δt. The corresponding angular phase rate is defined as $\omega_{CF} = \frac{\Delta\phi}{\Delta t}$. With this notation, the real part of this signal can be termed the in-phase (I) component, and the imaginary part the quadrature (Q) component. In this color flow study, ω_{CF} is chosen to be a function of the firing number (t_f) within the packet, the volume number (v), and the position in 3D space (x, y, z). Mathematically,

$$g(t_f, v, x, y, z) = e^{i\omega_{CF}(t_f,v,x,y,z)t} = I(t_f, v, x, y, z) + iQ(t_f, v, x, y, z) \tag{1}$$

For brevity, let $\boldsymbol{r} = [t_f \;\; v \;\; x \;\; y \;\; z]$ and $\boldsymbol{s} = [v \; x \; y \; z]$. The initial power, the power determined for each firing in a packet and evaluated at $\boldsymbol{r}$, is equivalent to

$$p(\boldsymbol{r}) = |g(\boldsymbol{r})|^2 = I^2(\boldsymbol{r}) + Q^2(\boldsymbol{r}). \tag{2}$$

If there are m firings in a packet, then the total power, per volume and pixel, is equal to:

$$P(\boldsymbol{s}) = \sum_{j=1}^{m} p(t_j, \boldsymbol{s}) \tag{3}$$

Equation (3) shows that the total power is the sum of powers that are treated as random variables. Therefore, their interdependency must be considered due to the finite beamwidth and likely dependency of voxels that are near each other. Additionally, power estimates for one voxel from one firing to the next are by design highly correlated. Otherwise, the phase change from firing to firing could not yield a meaningful velocity estimate. Since power at any given location is directly proportional to the amount of moving blood cells at that location [4], any change in the number of blood cells at one moment is correlated with the number of blood cells at the previous moment. We asserted that color flow power could be modeled as a gamma distributed random variable with distinct shape parameters for tissue and blood. The probability density function (PDF) of a gamma random variable X is

$$f_X(x;\,\alpha,\,\beta) = \frac{1}{\Gamma(\alpha)} x^{\alpha-1}\beta^{\alpha}e^{-\beta x}, \tag{4}$$

where Γ is the gamma function, α is the shape parameter, and β is the scale parameter. We started our investigation by considering IQ data derived power data of tissue and blood separately due to anticipated differences in their statistical properties. The gamma distribution was fitted to the calculated power histogram for each tissue and blood sample using the maximum likelihood estimation (MLE). The estimated shape parameters (α) and scale parameters (β) were computed for both simulation and experimental data. In this study, a sample corresponds to a single scalar color-flow power value computed at one spatial pixel location and one temporal realization (volume for simulation data or frame for experimental data). Power histograms were constructed by pooling these samples across selected spatial regions and across time, without temporal averaging. Having separate initial estimates of the shape parameters, i.e., for tissue and blood, we conducted the next analysis by considering the transition from blood to tissue. To this end, we moved laterally across power pixels and measured the shape parameter of the gamma distribution of all axial pixels for any given lateral position. For the lateral-transition analysis, two adjacent lateral positions were pooled at each step to construct the power histograms. In the simulation data, the blood-tissue boundary is sharply defined such that a single lateral pixel is entirely within either blood or tissue; pooling two neighboring lateral positions therefore enables explicit characterization of the statistical transition across the interface. This process was performed to investigate whether the measured shape parameters are discriminative between tissue and blood. At each lateral position, the estimated gamma PDF was superimposed on the histogram for qualitative comparison and the estimated shape parameters (α), and scale parameters (β) were collected.

Goodness-of-fit between empirical color flow power distributions and the fitted gamma model was evaluated using quantile–quantile (Q–Q) analysis rather than classical hypothesis tests. Formal goodness-of-fit tests such as Kolmogorov–Smirnov or Anderson–Darling assume independent samples, an assumption violated in color flow ultrasound data due to spatial correlation imposed by the system point-spread function and temporal correlation across frames and firings. Q–Q analysis provides a distribution-wide, assumption-light assessment of agreement by directly comparing empirical and theoretical quantiles, allowing systematic deviations to be visualized across low, mid, and high quantile ranges, including the distribution tail.

Q–Q analysis was applied to the first step of the analysis, where the objective is to validate the assumed statistical model for color flow power in representative blood and tissue regions. In this step, samples correspond to scalar power values at fixed spatial locations aggregated across time. The second step of the analysis focuses on the lateral transition across the blood–tissue interface, where local power histograms were constructed by aggregating two adjacent lateral positions at each step. Generating Q–Q plots for every lateral position would result in a large number of highly similar figures with incremental differences and limited additional insight. Instead, spatial changes across the interface were quantified through the lateral evolution of the fitted distribution parameters, which provides a compact and physically interpretable description of the transition.

Quantitative Q-Q agreement was measured using the mean absolute quantile error (MAQE),

$$MAQE = 1/n\sum_{i=1}^{n}|Q_{emp}(p_i) - Q_{theo}(p_i)| \tag{5}$$

where $Q_{emp}(p_i)$ represents the empirical quantile of the measured color flow power at quantile level p_i, and $Q_{theo}(p_i)$ represents the corresponding theoretical quantile obtained from the fitted gamma distribution. The p_i denotes uniformly spaced quantile levels with the interval [0.01, 0.99], and n is the total number of evaluated quantiles. In addition to full-range MAQE, a bulk-restricted MAQE (lower 95% of quantiles) and a tail-restricted MAQE (highest 5% of quantiles) were computed to separately assess agreement over the dominant distribution and deviations associated with rare high-power samples.

As the next verification measure, we calculated the empirical cumulative distribution function (ECDF) to represent the observed IQ data power at each step of our analysis without assuming any underlying parametric model. Then, we compared the ECDF against the theoretical cumulative distribution function (CDF) for the gamma distribution according to the following equation:

$$f_{theoretical}(x;\,\alpha,\,\beta) = \int_0^x \frac{1}{\Gamma(\alpha)} t^{\alpha-1}\beta^{\alpha}e^{-\beta t}dt, \tag{6}$$

Where Γ is the gamma function, α is the shape parameter, and β is the scale parameter. These parameters were collected from the gamma fitting. As a quantitative measure, the point-wise absolute error between the empirical and theoretical CDFs was estimated and the maximum absolute error (MAE) was recorded in each step of the analysis.

We note that power samples are not strictly independent due to temporal correlation across frames and firings and spatial correlation imposed by the finite beamwidth and point-spread function of the ultrasound system. These correlations arise because the same blood cells and tissue scatterers contribute to signals across nearby pixels (i.e., from shared speckle spots) and consecutive frames. The objective of this work is to characterize the empirical distribution of color flow power observed for blood and tissue under realistic imaging conditions. While such correlation reduces the effective number of independent samples and may increase estimator variance, it does not change the form of the single-sample distribution of color flow power being modeled.

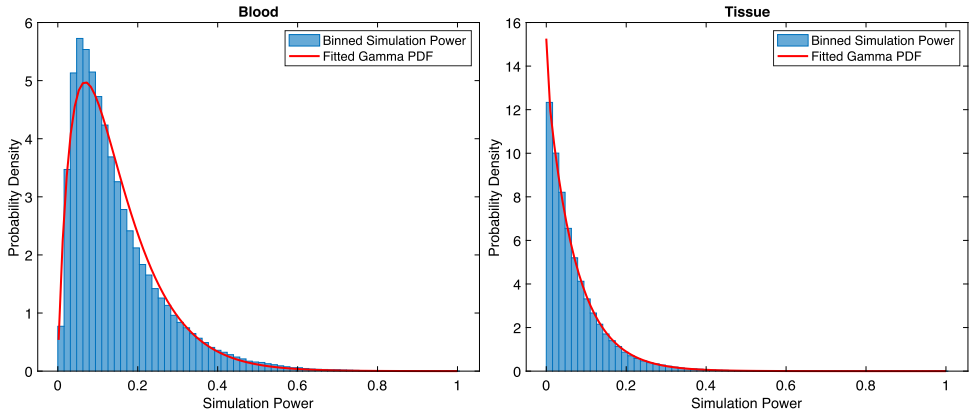

Figure 3. Example of the qualitative difference of gamma-based PDFs for simulation data. Power data was obtained from color flow firings IQ data. Left: Blood only with a gamma distribution. Right: Tissue only with an exponential distribution.

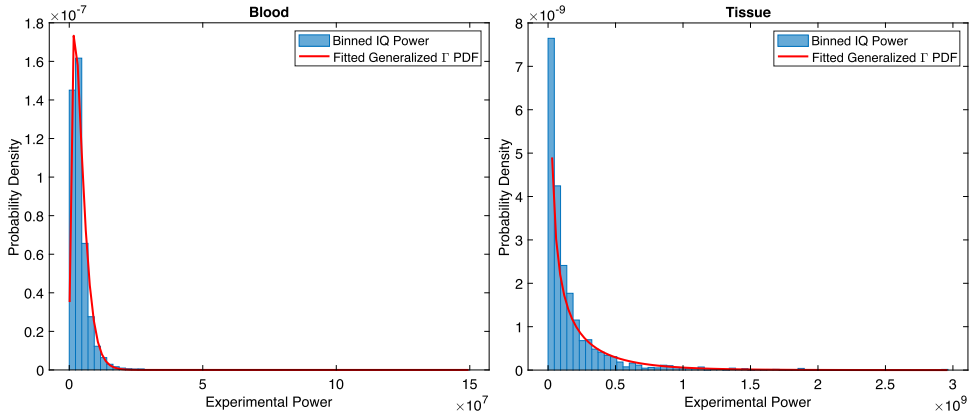

Figure 4. Example of the qualitative difference of gamma-based PDFs for experimental data. Power data was obtained from color flow firings IQ data. Left: Blood only with a gamma distribution. Right: Tissue only with an exponential distribution.

Table 1. Gamma shape parameter estimation using maximum likelihood estimation for color flow power of blood and tissue. The analysis was performed on simulation data and data from three physical experimental replications.

Data source	Tissue shape parameter	Blood shape parameter
Simulation	0.99	1.88
Experimental	0.69, 0.69, 0.63	1.95, 2.05, 1.95

3. Results

A qualitative comparison between the estimated gamma PDFs and their corresponding tissue and blood histograms are presented in figures 3 and 4 for simulation and experimental data, respectively. The shape parameters obtained are shown in table 1. Here, these parameters serve as an initial quantitative reference point with respect to their values exclusively for tissue and blood.

In this initial step, Q–Q analysis was used to evaluate the agreement between empirical color flow power distributions and the fitted gamma model under both simulation and experimental conditions. Agreement was quantified using measured MAQE, a bulk-restricted MAQE computed over the lower 95% of quantiles, and a tail-restricted MAQE computed over the highest 5% of quantiles, enabling separation of dominant distribution behavior from rare, high-power samples. The results are shown in figures 5 and 6 for simulation and experimental data respectively. Measured MAQE values are reported in table 2 for both simulation and experimental data.

The corresponding ECDFs and CDFs are shown in figures 7 and 8 for simulation and experimental data, respectively. These figures compare the point-by-point cumulative probabilities of the empirical data (ECDF) with the probabilities fitted by the gamma distribution (CDF). This comparison allows us to assess the fit across the entire range of the data, highlighting regions where the gamma model

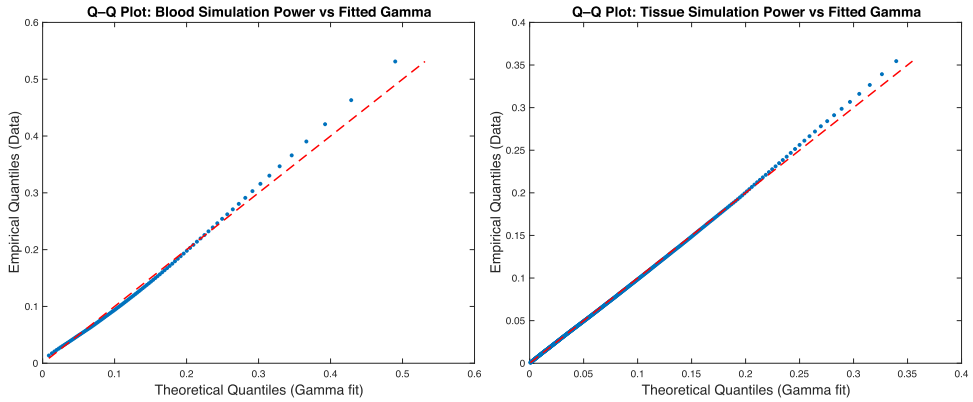

Figure 5. Left: Q–Q plot comparing empirical blood power quantiles from simulation data with theoretical quantiles from the fitted gamma distribution. The plot demonstrates close agreement across the dominant portion of the distribution, with deviations confined to the extreme upper tail. Right: Q–Q plot comparing empirical tissue power quantiles from simulation data with the fitted gamma distribution. The strong alignment with the diagonal across nearly the entire range indicates that tissue power statistics in simulation are well described by an exponential-like gamma model.

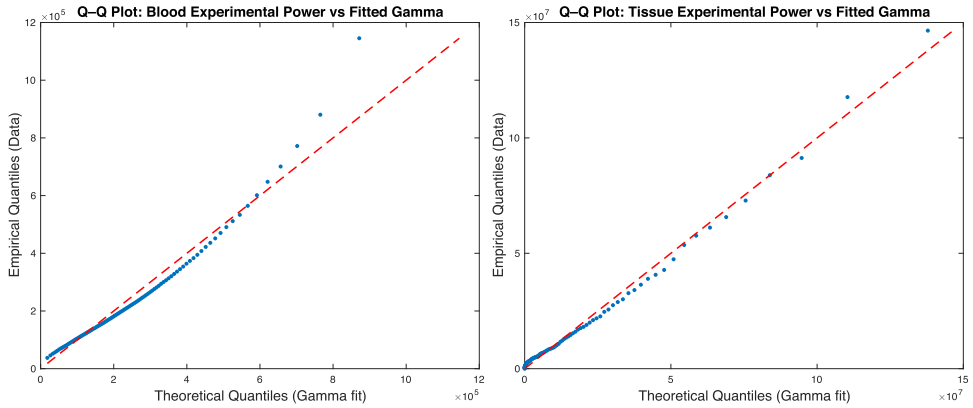

Figure 6. Left: Q–Q plot comparing empirical blood power quantiles from experimental data with the fitted gamma distribution. Agreement is observed across the bulk of the distribution, with deviations localized to the upper tail, corresponding to rare high-power samples in experimental acquisitions. Right: Q–Q plot comparing empirical tissue power quantiles from experimental data with the fitted gamma distribution. Broader deviations are observed, particularly in the upper tail, reflecting contributions from coherent clutter and elevational averaging. Despite these effects, the dominant statistical behavior is captured by the gamma model.

performs well and areas where it diverges from the empirical observations. A bar graph is provided to quantify the relative difference between empirical and theoretical data. Since ECDF values are given in fractions of 0 to 1, their difference is shown as a percentage. To further quantify the accuracy of the gamma distribution fit, we also calculated the MAE between ECDF and CDF and reported them in table 3.

The next step in the analysis was to evaluate the behavior of the gamma distribution across the lateral direction of the simulation and the physical phantom, with the aim of identifying the blood-tissue boundary. For this purpose, a gamma distribution was fitted to the histogram of all axial data at each lateral position. This approach allows us to examine changes in the gamma distribution parameters, particularly the shape parameter, as we move laterally across the phantom. The estimated shape parameters are shown in figure 9. These figures illustrate how the shape parameter could potentially assist in detecting the lumen boundary. To assess the fit quality at each lateral position, we measured the respective MAEs between the ECDF and the CDF. MAE values for simulation and experimental datasets are shown in figure 10. This analysis highlights the consistency of the gamma distribution model.

4. Discussion

According to figures 3 and 4, the fit appears to capture the general data shape and spread, indicating that the gamma distribution may be a suitable model for blood and tissue power histograms. This visual assessment is

Table 2. Measured values of MAQE, bulk-restricted MAQE, and tail-restricted MAQE for blood and tissue samples in simulation and three physical experimental replications.

Data source	Tissue MAQE	Tissue bulk-restricted MAQE	Tissue tail-restricted MAQE	Blood MAQE	Blood bulk-restricted MAQE	Blood tail-restricted MAQE
Simulation	2.07%	1.11%	15.47%	5.53%	3.83%	26.97%
Experimental	27.57%, 24.95%, 23.95%	13.95%, 12.64%, 11.92%	96.38%, 54.74%, 64.41%	17.22%, 12.84%, 12.23%	12.30%, 8.28%, 8.42%	61.49%, 70.53%, 54.32%

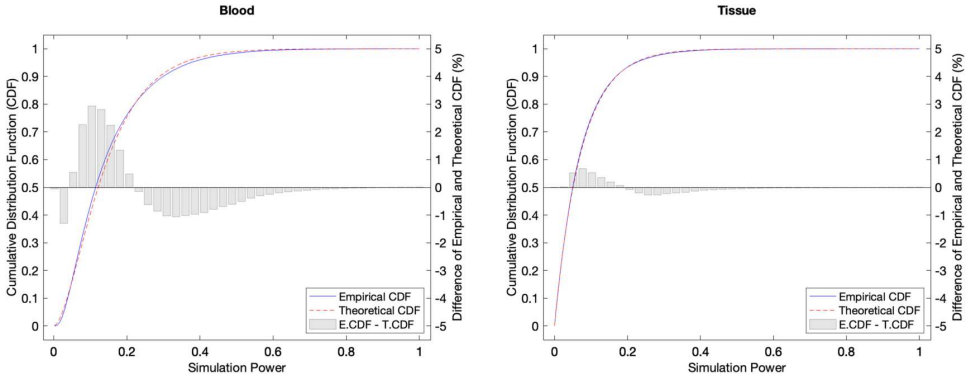

Figure 7. Gamma fit evaluation by comparing empirical and theoretical CDFs for simulation data. The %-difference of empirical and theoretical data is shown as a bar plot. Left: Comparison for color flow power of blood. Right: Comparison for color flow power of tissue.

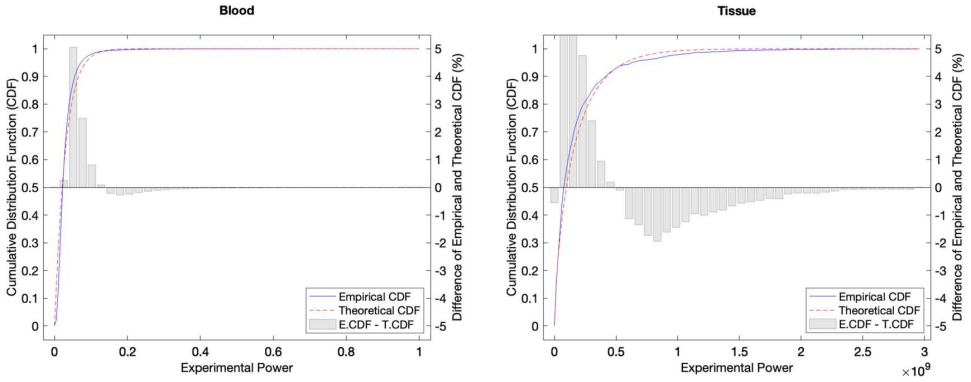

Figure 8. Gamma fit evaluation by comparing empirical and theoretical CDFs for experimental data. The %-difference of empirical and theoretical data is shown as a bar plot. Left: Comparison for color flow power of blood. Right: Comparison for color flow power of tissue.

Table 3. Calculated maximum absolute error (MAE) between estimated (modeled) and measured cumulative distribution functions (ECDF and CDF) for each blood and tissue samples of simulation data and data from three physical experimental replications.

Data source	Tissue MAE	Blood MAE
Simulation	0.01	0.03
Experimental	0.08, 0.07, 0.07	0.08, 0.07, 0.07

a crucial step in validating the appropriateness of the distribution model. Referring to equation (4), to understand the behavior of the gamma distribution with respect to x, we focus on the term $x^{\alpha-1}e^{-\beta x}$ as follows,

- For $\alpha = 1$, $f(x) = x^{\alpha-1}e^{-\beta x} = \beta x^0 e^{-\beta x} = \beta e^{-\beta x}$, thus the PDF is non-zero and finite at $x = 0$ ($f(0) = \beta$). For $x > 0$, the distribution falls off exponentially, and the decay rate is determined by the scale parameter β.
- For $\alpha < 1$, the term $x^{\alpha-1} \to \infty$ as $x \to 0$ since $e^{-\beta x} \to 1$. Thus, the PDF reaches infinity as x approaches zero. For $x > 0$, there is a high concentration of the probability density near zero. Therefore, the gamma PDF peaks very sharply near $x = 0$, and rapidly decays at larger values of x. According to the results presented in table 1 and illustrated in figure 9, all estimated tissue shape parameters are less than or equal to 1. Histograms for both simulation and experimental data further confirms such behavior of the tissue sample distribution (figures 3 and 4).
- For $\alpha > 1$, the term $x^{\alpha-1} \to 0$ as $x \to 0$. In this case, the distribution has less density near x=0, and the PDF peak shifts away from zero. For small values of x near zero, $x^{\alpha-1}$ governs the growth of the PDF until x reaches the mode of the PDF. Subsequently, the distribution begins to flatten due to the exponential decay term $e^{-\beta x}$. This behavior represents a gamma PDF. According to the results

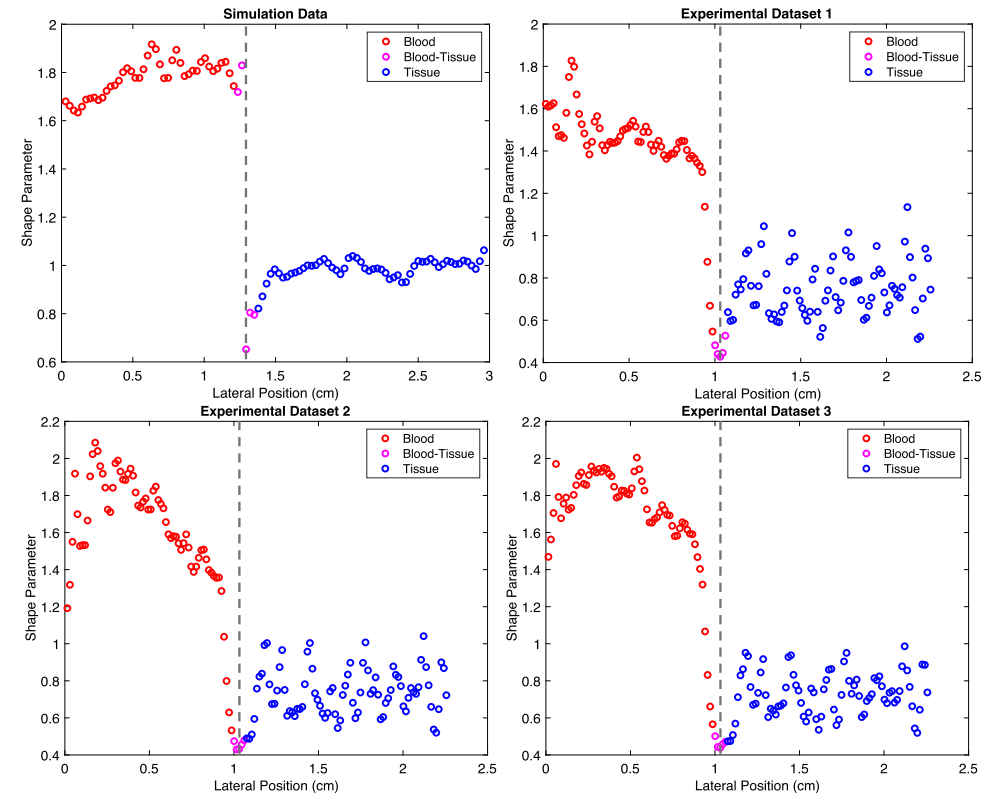

Figure 9. Estimated shape parameters across lateral positions are presented for one simulation and three experimental datasets. The top-left panel shows the estimated shape parameters for simulation data and the other three panels show the estimated shape parameters for the three experimental datasets. Blood samples are colored in red, tissue samples in blue, and the blood-tissue boundary in magenta. The dotted line represents the approximate position of the blood-tissue boundary.

presented in table 1 and illustrated in figure 9, all estimated blood shape parameters are greater than 1. Histograms for both simulation and experimental data further confirm the nature of the blood sample distribution (figures 3 and 4).

According to figures 5 and 6 and reported MAQE values in table 2, for the simulation data, bulk-restricted MAQE values were low for both tissue (1.11%) and blood (3.83%), indicating close alignment between empirical and theoretical quantiles across the dominant portion of the distribution. Deviations were primarily confined to the upper tail, corresponding to the upper-right region of the Q–Q plots, with tail-restricted MAQE values of 15.47% for tissue and 26.97% for blood. Experimental data exhibited larger deviations, but consistent trends were observed across all three independent acquisitions. For blood, bulk-restricted MAQE values ranged from 8.28% to 12.30%, while tail-restricted MAQE values ranged from 54.32% to 70.53%, indicating that discrepancies are largely restricted to infrequent, high-power samples potentially arising from momentary constructive interference contributions of moving scatterers and motion-induced temporal decorrelation. For tissue, bulk-restricted MAQE values ranged from 11.92% to 13.95%, with substantially larger tail-restricted MAQE values ranging from 54.74% to 96.38%. These broader deviations reflect increased variability associated with coherent clutter and elevational averaging from stationary scatterers. Despite these deviations, the consistent separation between low bulk-restricted MAQE and elevated tail-restricted MAQE across all datasets demonstrates that the gamma model captures the dominant statistical behavior of color flow power in both simulation and experimental data. Model mismatches are localized to physically interpretable high-quantile regions rather than indicating a global failure of the assumed distributional model.

The close alignment between ECDF and CDF in figures 7 and 8 supports the suitability of the gamma distribution for modeling these data. MAE values provided in table 3 indicate a close fit to the empirical data, with all values presented as proportions (i.e., an MAE of 0.01 indicates an average 1% difference between the empirical and modeled distributions).

Color flow power is formed by summing squared in-phase and quadrature signal components across multiple firings, resulting in a non-negative quantity whose statistics depend on the number of effectively

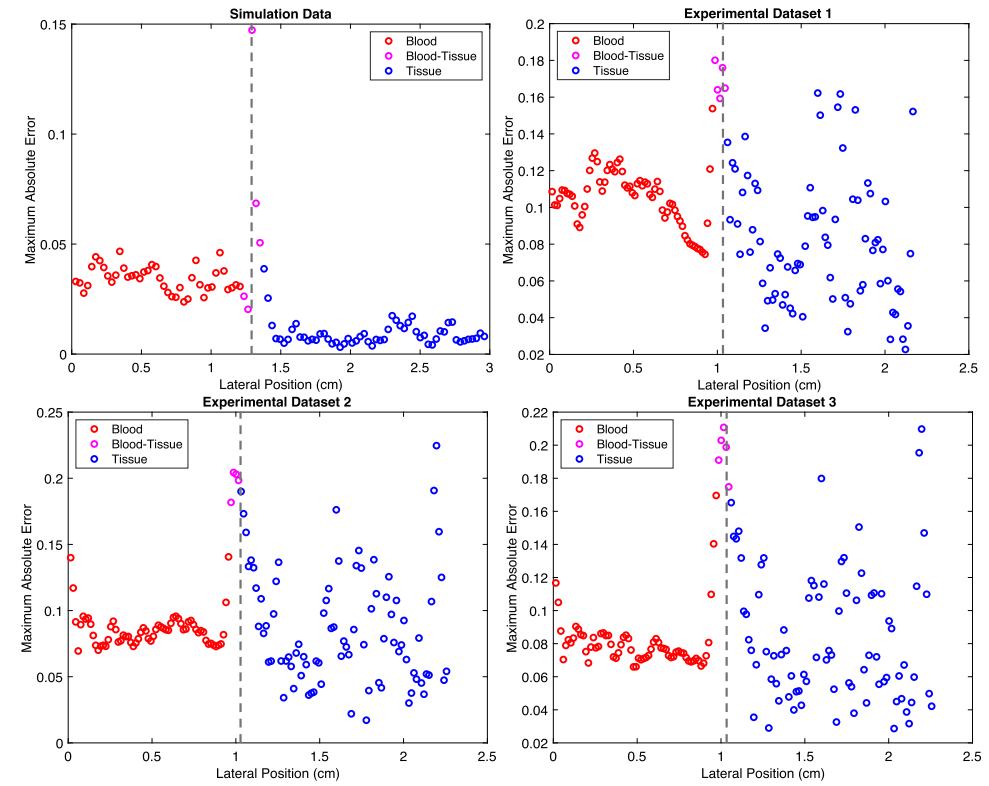

Figure 10. Maximum absolute error between the empirical cumulative distribution function (ECDF) and the actual cumulative distribution function (CDF) at each lateral position for simulation data (top-left) and for the three experimental datasets.

independent scatterer contributions. Blood and tissue differ fundamentally in this respect. In blood, scatterers are moving and thus continuously enter and leave the point-spread function, leading to temporal decorrelation and a larger number of scatterers effectively contributing. In contrast, tissue scatterers are largely stationary and are repeatedly observed across firings and frames, resulting in a fixed number of independent scatterers contributing. The gamma distribution provides a flexible statistical model for such summed quantities, and its shape parameter can be interpreted as an effective descriptor of scattering dynamics rather than a unique, one to one mapping to a single physical parameter. These differences in scattering behavior led to distinct ranges of shape parameters for blood and tissue, enabling their statistical discrimination in color flow imaging.

The observed differences between the estimated blood and tissue shape parameters in both simulation and experimental data, as depicted in figure 9, along with the values in table 1, align with theoretical expectations that were discussed above. Blood shape parameters are uniformly larger than those of tissue. There is a pronounced decrease in the shape parameter at the blood/tissue interface when transitioning from blood into tissue. This phenomenon can be attributed to the change in the scattering environment, such as (a) a 40 dB increase in backscatter in tissue versus blood; and (b) temporally changing speckle patterns in blood throughout the color flow packet versus stationary speckle in soft tissue.

We observe that the estimated gamma PDF derived shape parameters are more discriminative between blood and tissue in the simulation setting than compared to the experimental data. Potential contributors to this difference include: (a) idealized (blood and tissue) scatterer distributions in the simulation environment versus potential aggregation of physical scatterers (which we tried to actively avoid by gently pre-stirring for 3 hours and circulating in the phantom for one hour to also avoid bubbles); (b) simulation data do not incorporate system and environmental artifacts, such as electronic noise, ensuring high-dynamic range data with minimal signal-to-noise ratio degradation. Moreover, the presence of a finite elevational beam width when imaging the flow phantom may introduce out-of-plane tissue signal, i.e., clutter, while the simulation assumes an absence of such. This may contribute to additional backscatter, affecting the blood IQ data power distribution with stationary speckle, and as a result, may obscure the distinction between blood and tissue in the histograms. Despite these limitations and differences between the nature of simulation and physical

experiment, the estimated shape parameters follow theoretical expectations as discussed above and discriminate between blood and tissue using IQ power data. Moreover, calculated shape parameters across lateral positions for all three experimental datasets represent the same pattern as shown in figure 9. This demonstrates reproducibility.

The flow phantom used in this study was designed as a simplified model for proof-of-concept validation rather than to replicate a specific organ or vascular geometry. This approach allows isolation of the fundamental statistical differences between blood and tissue color flow power without confounding effects from organ shape, vessel curvature, or complex flow patterns. Because the proposed method relies on local power statistics derived from scatterer motion, it is theoretically independent of organ geometry. The simplified phantom provides a controlled baseline for validating the framework, with future work focusing on extension to organ-specific geometries and *in vivo* applications.

The proposed framework relies on local color flow power statistics rather than angle-dependent velocity estimates. Therefore, it is robust to changes in probe orientation. Probe rotation affects spatial sampling but does not fundamentally change the power-based statistical characteristics used for blood-tissue discrimination. Evaluation across multiple imaging angles and freehand probe motion represents an important extension of this work and will be investigated in future studies. Therefore, while this setup provides a clear foundation for hypothesis testing, we acknowledge that real clinical environments introduce additional complexities such as wall filter settings, transducer and patient motion, and varying machine parameters. These factors can influence signal characteristics and may affect the robustness of the statistical quantities derived here. As a next step, our framework should be extended to clinical data, where we will assess model resilience. This progression from idealized to practical scenarios is essential to ensure the method's applicability in clinical practice.

In the present study, the proposed statistical modeling framework is implemented as an off-line analysis to enable validation and interpretation of color flow power statistics. Nevertheless, the required computations including the local power estimation and gamma parameter fitting, are computationally inexpensive relative to current hardware and can therefore be implemented without concerns about significant performance loss. This makes the approach suitable for real-time application in clinical ultrasound systems. Future work will focus on clinical evaluation of the proposed method and real-time operation.

For future applications, the color flow power signal can be influenced by blood cell dynamics, such as the shape, size, and concentration of cells in the blood. For example, abnormally shaped cells in sickle cell anemia, or changes in cell size and hemoglobin content in thalassemia, could result in variations in blood flow dynamics. Sickle-shaped cells can lead to blockages in small vessels. A deviation from expected gamma distribution patterns can model flow characteristics through changes in the color flow power signal. Assessing the gamma distribution parameters could be useful in evaluating blood flow behavior and inferring changes in blood cell density. In conditions like polycythemia, with increased RBC concentration, altered color flow signals might be observed due to higher blood viscosity, and this could be reflected in the power distribution of the color flow ultrasound. In general, the application of investigating gamma distribution shape parameters in color flow power can be extended to potentially better monitor disease progression across various conditions.

5. Conclusion

This study investigated whether the IQ data-based power derived from color flow firings follows a gamma distribution and exhibits distinct shape parameters for blood and tissue domains. Initially, theoretical probability density functions were derived and confirmed. Subsequently, the investigation of the blood-tissue transition provided evidence of potential effectiveness. Finally, the simulation results were also validated by experimental data; demonstrating that the estimated shape parameters are discriminative between blood and tissue. This approach provides a statistical framework for interpreting blood flow characteristics in various vascular conditions.

Funding

This work was in part supported by internal funding P/G U086090.

Author contributions

Atefeh Abdolmanafi: Conceptualization, Data curation, Formal analysis, Investigation, Methodology, Software, Validation, Visualization, Writing—original draft.

Jonathan M Rubin: Conceptualization, Writing—review & editing, Supervision.

Stephen Z Pinter: Data curation, including data strategy and execution, and flow phantom development, Writing—review & editing.

J. Brian Fowlkes: Writing—review & editing.

Oliver D Kripfgans: Conceptualization, Data curation, Funding acquisition, Writing—review & editing, Supervision, Resources.

Data availability statement

The data cannot be made publicly available upon publication because no suitable repository exists for hosting data in this field of study. The data that support the findings of this study are available upon reasonable request from the authors.

References

[1] Forsberg F 2020 Three-dimensional US measurements of blood flow: one step closer to clinical practice *Radiology* **296** 671–2

[2] Beach K W *et al* 1997 Ultrasonic color flow mapping: the visualization of four-dimensional cardiac and vascular flow phenomena using two dimensions and 'real time' *Ultrasound Med. Biol.* **23** 347–63

[3] Ferrara K and DeAngelis G 1997 Color flow mapping Ultrasound in *Medicine & Biology* **23** 321–45

[4] Rubin J M, Bude R O, Carson P L, Bree R L and Adler R S 1994 Power Doppler US: a potentially useful alternative to mean frequency-based color Doppler US *Radiology* **190** 853–6

[5] Kennel P, Dichamp J, Barreau C, Guissard C, Teyssedre L, Rouquette J, Colombelli J, Lorsignol A, Casteilla L and Plouraboué F 2020 From whole-organ imaging to in-silico blood flow modeling: a new multi-scale network analysis for revisiting tissue functional anatomy *PLoS Comput. Biol.* **16** e1007322

[6] Kim H J, Rundfeldt H C, Lee I and Lee S 2023 Tissue-growth-based synthetic tree generation and perfusion simulation *Biomech. Model. Mechanobiol.* **22** 1095–112

[7] Destrempes F and Cloutier G 2010 A critical review and uniformized representation of statistical distributions modeling the ultrasound echo envelope *Ultrasound Med. Biol.* **36** 1037–51

[8] Shankar P M 2000 A general statistical model for ultrasonic backscattering from tissues *IEEE Trans. Ultrason. Ferroelectr. Freq. Control* **47** 727–36

[9] Shankar P M 2001 Ultrasonic tissue characterization using a generalized nakagami model *IEEE Trans. Ultrason. Ferroelectr. Freq. Control* **48** 1716–20

[10] Shankar P M 2003 A compound scattering pdf for the ultrasonic echo envelope and its relationship to K and Nakagami distributions *IEEE Trans. Ultrason. Ferroelectr. Freq. Control* **50** 339–43

[11] Nillesen M M, Lopata R G, Gerrits I H, Kapusta L, Thijssen J M and de Korte C L 2008 Modeling envelope statistics of blood and myocardium for segmentation of echocardiographic images Ultrasound in *Medicine & Biology* **34** 674–80

[12] Damerjian V, Tankyevych O, Souag N and Petit E 2014 Speckle characterization methods in ultrasound images–a review *Irbm* **35** 202–13

[13] Al-Kadi O S, Chung D Y, Carlisle R C, Coussios C C and Noble J A 2015 Quantification of ultrasonic texture intra-heterogeneity via volumetric stochastic modeling for tissue characterization *Med. Image Anal.* **21** 59–71

[14] Oelze M L and Mamou J 2016 Review of quantitative ultrasound: envelope statistics and backscatter coefficient imaging and contributions to diagnostic ultrasound *IEEE Trans. Ultrason. Ferroelectr. Freq. Control* **63** 336–51

[15] Teh B G and Cloutier G 2000 Modeling and analysis of ultrasound backscattering by spherical aggregates and rouleaux of red blood cells *IEEE Trans. Ultrason. Ferroelectr. Freq. Control* **47** 1025–35

[16] Müller M, Ciccotti P, Reiche W and Hagen T 2001 Comparison of color-flow Doppler scanning, power Doppler scanning, and frequency shift for assessment of carotid artery stenosis *Journal of Vascular Surgery* **34** 1090–5

[17] Wagner R F, Insana M F and Brown D G 1987 Statistical properties of radio-frequency and envelope-detected signals with applications to medical ultrasound *J. Opt. Soc. Am.* **4** 910–22

[18] Bernard O, Touil B, D'hooge J and Friboulet D 2007 Statistical modeling of the radio-frequency signal for partially-and fully-developed speckle based on a generalized gaussian model with application to echocardiography *IEEE Trans. Ultrason. Ferroelectr. Freq. Control* **54** 2189–94

[19] Kripfgans O D, Rubin J M, Pinter S Z, Jago J, Leichner R and Fowlkes J B 2019 Partial volume effect and correction for 3-D color flow acquisition of volumetric blood flow *IEEE Trans. Ultrason. Ferroelectr. Freq. Control* **66** 1749–59

[20] Jensen J A and Svendsen N B 1992 Calculation of pressure fields from arbitrarily shaped, apodized, and excited ultrasound transducers *IEEE Trans. Ultrason. Ferroelectr. Freq. Control* **39** 262–7

[21] Kasai C 1986 Real-time two-dimensional blood-flow imaging using an autocorrelation technique *IEEE Transactions on Ultrasonics Ferroelectrics and Frequency Control* **33** 94–94

[22] Namekawa K, Kasai C, Tsukamoto M and Koyano A 1983 Realtime bloodflow imaging system utilizing auto-correlation techniques *Ultrasound Med. Biol.* **Suppl 2** 203–8 PMID: 17092547

[23] Ryan L K and Foster F S 1997 Tissue equivalent vessel phantoms for intravascular ultrasound *Ultrasound Med. Biol.* **23** 261–73

[24] Kasai C, Namekawa K, Koyano A and Omoto R 1985 Real-time two-dimensional blood flow imaging using an autocorrelation technique *IEEE Trans. Sonics Ultrason.* **32** 458–64